



Modulating the oxidative active species by regulating the valence of palladium cocatalyst in photocatalytic degradation of ciprofloxacin

Fa Guo, Hao Zhang, Hui Li, Zhurui Shen^{*}

School of Materials Science and Engineering, Nankai University, Tianjin 300350, China



ARTICLE INFO

Keywords:

Metal cocatalyst
Valence regulation
Surface states
Oxidative active species
Contribution modulating

ABSTRACT

Nano-structured metal cocatalysts are easy to be oxidized and form mixed valences and interfaces which would facilitate the catalytic performance in previous studies. Herein, as an example in photocatalysis, three kinds of Pd cocatalysts with various valence distributions (PdO70-Pd30/CN, PdO50-Pd50/CN and PdO30-Pd70/CN) were loaded on g-C₃N₄ nanosheets with the close loading amounts (~1 wt%) and uniform sizes (2–3 nm). Then, the results of the photocatalytic degradation of ciprofloxacin showed that the generated oxidative active species are highly related to the distribution of palladium valence. Pd²⁺ (PdO) benefits the production of O₂[·], while Pd⁰ benefits the production of h⁺. The theoretical simulations revealed that surface states e.g., electron distribution and the adsorption ability of O₂ on different Pd species determined the production of O₂[·] and h⁺. Besides, PdO50-Pd50/CN showed the best performance for degrading ciprofloxacin, due to the joint action of O₂[·] and h⁺ in the CIP degradation.

1. Introduction

For decades, metal cocatalysts have significantly improved the electronic structure, energy states and reaction stability of catalysts, and thus are widely used in various important heterogeneous catalytic reactions, including thermal catalysis, electrocatalysis and photocatalysis [1–4]. Amongst, typical metal cocatalysts include noble metals, e.g., Pt, Pd and Au, as well as non-precious metals e.g., Fe, Cu and Ni [5–7]. Recently, when fabricated into nanostructures, these metal cocatalysts have been found to be easily oxidized to form mixed valence states in the process of preparation or reaction [8,9]. For one thing, it brings uncertainty to its role as a cocatalyst, especially during long-term reactions. For another, several pioneering works showed that the mixed valence of the elements and the resulting interface in the nanoparticles can effectively modulate the electronic structure of the catalyst or improve the key steps of the catalytic reaction, thus promoting the occurrence of the catalytic reaction. For example, Su et al. reported the deposition of Pt/PtO phase mutation nanodot promoter on TiO₂, where the presence of Pt²⁺ provided additional photocatalytic hydrogen production active sites and effectively suppressed the reverse reaction of H₂ evolution [10]. Wang et al. found that the morphology of the CeO₂ support can significantly modulate the valence distribution of palladium cocatalyst, in which Pd²⁺ facilitates the catalytic oxidation of CH₄, while

Pd⁰ and Pd⁴⁺ do not directly contribute to the oxidation of methane [11]. Liang et al. prepared a PdO-Pd mixed valence cocatalyst on carbon nanotubes and proved that the interface formed between palladium oxide and palladium was the effective zone for electrocatalytic activation of N₂ toward an optimal yield of ammonia [12]. Among the many substrate materials, graphitic carbon nitride (g-C₃N₄) presents the advantages of simple synthesis, appropriate band gap, visible-light response and good chemical stability. Its layered structure and abundant surface-active sites make it a good basic material for loading metal cocatalysts [13]. Based on the above work and considering the universality of mixed valence phenomena in the actual synthesis and reaction process, it is necessary to further utilize the mixed valence metal cocatalysts in the new reaction system of carbon nitride materials, and explore its working mechanism.

In recent years, the unreasonable emission of antibiotics in the environment has attracted extensive attention [14–17]. Ciprofloxacin (CIP), one of the third-generation quinolone antibiotics, is widely used in the treatment of infectious diseases. Meanwhile, CIP is widely exposed to the water environment, causing harm to human health and the ecological environment [18–20]. However, traditional physical separation technology, biological methods and other water treatment technologies cannot effectively remove these antibiotics [21,22]. Therefore, advanced oxidation processes (AOPs) are regarded as having

* Corresponding author.

E-mail address: shenzhurui@nankai.edu.cn (Z. Shen).

potential due to their stronger direct oxidation capacity and better mineralization ability of antibiotics by producing oxidative active species ($\cdot\text{OH}$, O_2^- , h^+ and H_2O_2 et al.) [23–26]. Amongst, photocatalytic degradation of antibiotics is considered as a candidate strategy to effectively produce oxidative active substances through sunlight [27–30]. In this process, the sorts and ratio of generated active species were found to significantly affect the efficiency and pathway of pollutant degradation, which actually determine the environmental implications of the catalyst [31,32]. For example, Zhang et al. realized the non-toxic hydroxylation of atrazine by introducing thiosulfate species under acidic conditions, avoided the toxic intermediates produced in the separate-OH degradation path, and improved the biodegradability [33]. However, to date, it is still a great challenge to rationally regulate the sorts and ratios of generated active species, via the modulation of catalysts.

In these regards, palladium nanoparticles with different valence distributions were prepared and supported on carbon nitride photocatalysts as the new cocatalysts. Then, taking the photocatalytic degradation of CIP as a model reaction, the studies have been performed focusing on how the valence distribution of palladium affects the oxidative active species generated during the photocatalytic degradation of CIP. Via the series of control experiments and multiple spectroscopic analysis, the results showed that: (I) with the close particle size and loading amount, the sorts/ratio of generated oxidative active species were highly related to the distribution of valence of palladium, When Pd^{2+} (PdO) dominated the cocatalyst, O_2^- was the main active species. While in Pd^0 dominated cocatalyst, h^+ became the main active species. (II) The theoretical simulations revealed that surface states e.g., electron distribution and the adsorption ability of O_2 on different Pd species were the main reasons affecting the production of O_2^- and h^+ . (III) PdO50-Pd50/CN showed the best performance for degrading the ciprofloxacin, which was attributed to the joint action of O_2^- and h^+ .

2. Materials and methods

2.1. Preparation of $\text{g-C}_3\text{N}_4$ nanosheet and PdO-Pd/CN photocatalyst

The urea (15 g) was placed in the furnace and maintained at 550 °C (heating rate 5 °C/min) for 2 h to prepare $\text{g-C}_3\text{N}_4$ nanosheets according to previous literature [34]. Three palladium cocatalysts (PdO-Pd/CN) with different valence distributions were synthesized through three simple wet chemical routes. In a typical process, 200 mg $\text{g-C}_3\text{N}_4$ was added to 150 ml distilled water under ultrasonication for 1 h. Then, 1.93 ml of k_2PdCl_6 solution (Pd concentration of 1.048 mg/ml) was dropped into the mixture and stirred continuously for 15 min to obtain the precursor solution. Next, in the first synthesis route, 20 ml hydrogen peroxide was added to the precursor solution and stirred for 15 min. The mixed solution was washed and centrifuged after a water bath at 70 °C for 2 h, and dried under vacuum at 60 °C, and the obtained powder material was named PdO70%-Pd30%/CN. In the second synthetic route, the precursor solution was stirred without adding other reagents for 15 min, then bathed in water at 70 °C for 2 h, and the precipitate obtained by washing and centrifugation was vacuum dried at 60 °C. The final powder was named PdO50%-Pd50%/CN. In the third synthetic route, firstly, the precursor solution was bathed in water at 70 °C for 2 h, then 10 ml NaOH solution (1 M) was added to adjust the PH to 10, stirred for 15 min, and then excess NaBH₄ was added for the reaction. Finally, the powder obtained by washing, centrifugation and vacuum drying (60 °C) was named PdO30%-Pd70%/CN.

2.2. Characterizations

The morphology and microstructure of the samples were observed with Scanning electron microscopy (SEM, JSM-7800 F, 15KV) and Transmission electron microscopy (TEM, JEM-2800, 200KV). The crystalline structures were characterized by X-ray Diffraction (XRD) with

monochromatized Cu K α radiation (Rigaku Smart Lab 3 kW). The FTIR profiles were tested by INVENIO Fourier Transform Infrared Spectrometer. During the test, the ratio of the sample to potassium bromide is 1:100. The X-ray photoelectron spectroscopic (XPS) analysis was recorded on a Thermo Scientific ESCALAB 250Xi with an Al Ka radiation source. The Brunauer-Emmett-Teller (BET) specific surface areas and pore volume were determined from N₂ adsorption-desorption isotherms which were collected with a TriStar II 3020r at 78 K. Photoluminescence (PL) spectra were recorded by a fluorescence spectrometer (FLS-1000) with excitation wavelength of a 350 nm at room temperature. The photo-absorption performance of the materials was revealed by UV-Vis DRS with barium sulfate as a reference on a Shimadzu UV-2450 spectrometer. The photoelectrochemical performance was tested by a Chi660E electrochemical workstation with a three-electrode cell. The standard Ag/AgCl electrode and platinum electrode were used as the reference electrode and the counter electrode, respectively. The fabrication process of working electrodes was as follows: 10 mg of the photocatalyst was dispersed in the mixed solution containing 20 μL Nafion, 0.5 ml ethanol and 0.5 ml deionized water. Then, the suspension was coated on ITO glass (10 *20 *1 mm) and evaporated and dried at 40 °C. 0.2 M Na₂SO₄ solution and a 300 W Xe lamp were used as the electrolyte and light source. To detect active species in materials, the Bruker A300-10 spectrometer was used for electron spin resonance (ESR) testing. Note that O_2^- can be captured by DMPO, while h^+ can be captured by TEMPO (the concentration of h^+ is reflected by detecting the intensity of the TEMPO peak [35,36]). Total organic carbon (TOC) was collected via a Multi-N/C 2100 S. The mass fractions of Pd were measured by Agilent ICPOES730. Degradation intermediates of CIP were analyzed by HPLC-MS (Thermo ULTIMATE3000 UHPLC and Q EXACTIVE MS).

2.3. Photocatalytic performance measurement

The photoactivity of the photocatalyst was detected by the degradation of ciprofloxacin (CIP) under a 300 W Xe lamp with the main wavelength of 290–800 nm. On this basis, the photon flux of 22.5 mW/cm² was obtained on the surface of the reaction solution using the optical power meter. All subsequent photocatalytic degradation experiments were completed on this basis without any wavelength modification methods (such as filters). In a typical process, 25 mg photocatalyst was added into 50 ml 10mgL⁻¹ CIP solution. The above mixture was magnetically stirred in the dark for 30 min to achieve adsorption equilibrium, and then illuminated for 2 h. Next, 5 ml of the reaction solution was collected and filtered (0.22 μm filter membrane) at a fixed time point. The concentration of CIP solution was tested by using P4 UV-vis spectrophotometer at the absorption wavelength of 279 nm. The scavengers of O_2^- , h^+ , H_2O_2 , $\text{O}_2\cdot\text{OH}$ and e are TEMPOL, ammonium oxalate (AO), catalase (CAT), carotene, isopropanol (IPA) and KBrO₃, respectively (with all concentrations of 1 mM).

2.4. Theoretical calculation method

The present first principle DFT calculations are performed by the Vienna Ab initio Simulation Package (VASP) with the projector augmented wave (PAW) method. The exchange-functional is treated using the generalized gradient approximation (GGA) of the Perdew-Burke-Ernzerhof (PBE) functional. The energy cut-off for the plane wave basis expansion was set to 450 eV and the force on each atom less than 0.05 eV/Å was set for the convergence criterion of geometry relaxation. Grimme's DFT-D3 methodology was used to describe the dispersion interactions. The Brillouin zone was sampled with a gamma-centered grid $1 \times 1 \times 1$ throughout all the computational processes. The self-consistent calculations apply a convergence energy threshold of 10–5 eV. A 15 Å vacuum space along the z direction was added to avoid the interaction between the two neighboring images.

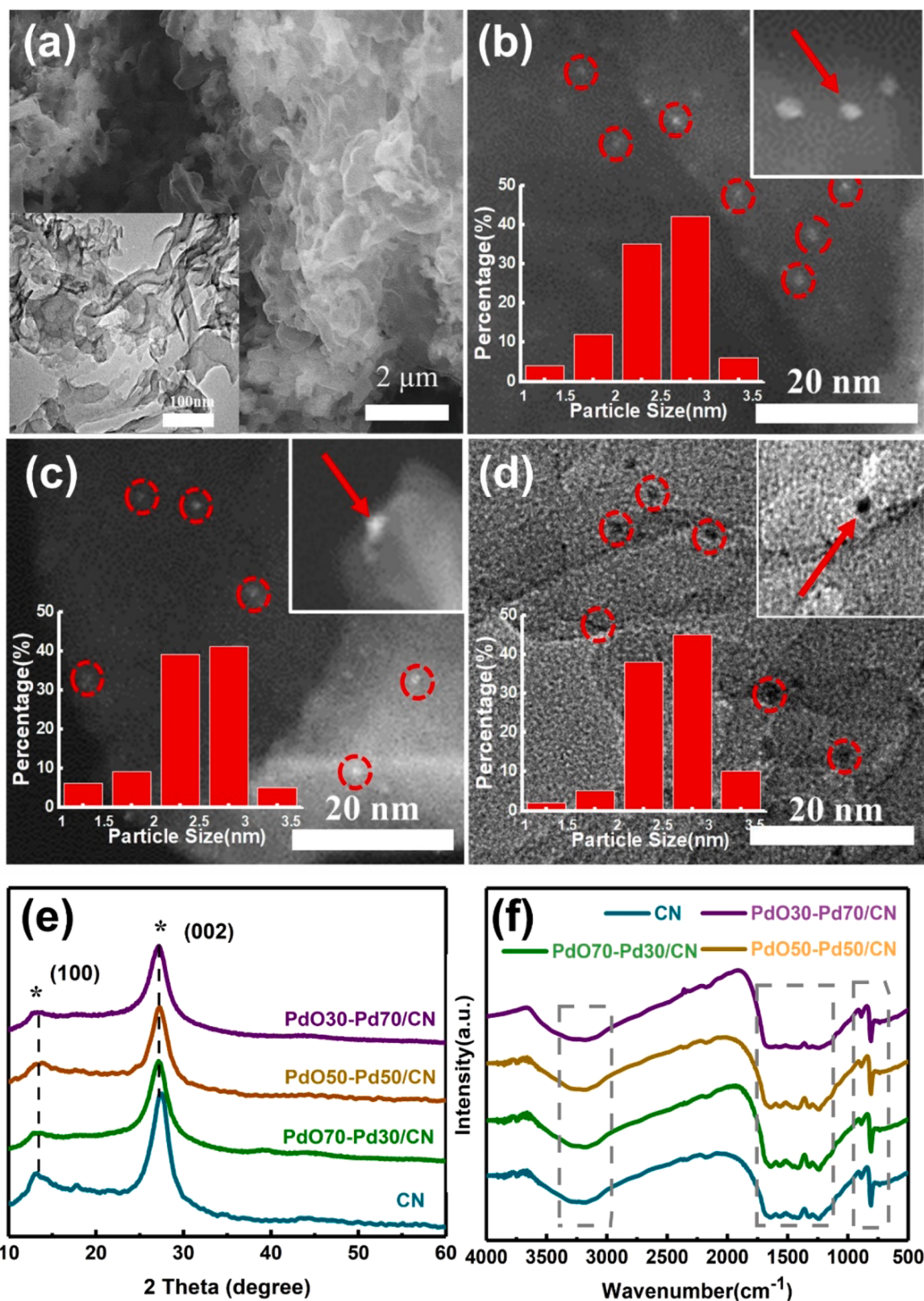


Fig. 1. (a) SEM images of $\text{g-C}_3\text{N}_4$; TEM images and corresponding histograms of palladium species size distribution of (b) $\text{PdO}_{70}\text{-Pd}_{30}/\text{CN}$, (c) $\text{PdO}_{50}\text{-Pd}_{50}/\text{CN}$ and (d) $\text{PdO}_{30}\text{-Pd}_{70}/\text{CN}$; (e) XRD patterns and (f) FTIR spectra of samples.

Table 1
ICP-OES results of Pd content.

Sample	Nominal loading (wt%)	Experimental loading (wt%)
PdO70-Pd30/CN	1.000	1.08
PdO50-Pd50/CN	1.000	0.91
PdO30-Pd70/CN	1.000	1.03

3. Results and discussion

3.1. Microstructure and chemical natures of the as-prepared Pd based catalysts

Three kinds of g-C₃N₄(CN) materials with different PdO-Pd ratios were designed and synthesized, which were close in basic morphology, particle size, loading amount, substrate structure, adsorption properties, photoelectric properties and so on. According to the percentages of PdO and Pd, the three materials are named PdO70-Pd30/CN, PdO50-Pd50/CN and PdO30-Pd70/CN, respectively.

To verify the successful preparation of the three PdO-Pd/CN materials, the micro morphologies of the materials were observed by transmission electron microscopy. Graphitic carbon nitride (CN) was formed by polymerization of urea and had a sheet structure (Fig. 1(a)). Palladium species on PdO-Pd/CN materials presented uniformly dispersed 2–3 nm particles as shown in Fig. 1(b)–(d). The ICP-OES results (Table 1)

showed that the actual contents of palladium species in the materials were close to 1%. At the same time, the EDS spectrum (Fig. S1) also verified the existence of Pd and O on the PdO-Pd/CN materials. Moreover, as shown in the XRD pattern of Fig. 1(e), two diffraction peaks at 20 of 13.5° and 27.4° were observed for all samples, which were ascribed to the characteristic (002) and (100) peaks of CN nanosheets. Slightly, the diffraction peak of (002) shifted to a lower angle after the introduction of PdO-Pd, indicated that the slightly increase of layer spacing due to the Strong-Metal-Support-Interaction effect between palladium and support material. [37,38]. But, the changes of (002) peaks for all the three palladium enhanced catalysts were basically the same, indicating that this effect not mainly contribute to their differences in the photocatalytic performance. No peaks related to palladium species were found in the XRD patterns of all materials attributed to the low Pd loading. The FTIR spectra of all samples are shown in Fig. 1(f), in which the absorption band of 800 cm⁻¹ corresponds to the bending vibration of nitrogen-containing heterocycles, the absorption band at 1200–1750 cm⁻¹ corresponds to the stretching vibration of aromatic carbon nitrogen rings, and the absorption band of 3000–3500 cm⁻¹ corresponds to the stretching vibration of N-H. Based on the FTIR results, the doping of PdO-Pd had no effect on the basic structure of the carbon nitride substrate [39]. All these results proved that the palladium cocatalyst with uniform particles and the same loading amount was loaded on the unchanged CN base material.

To further confirm the surface element composition and chemical

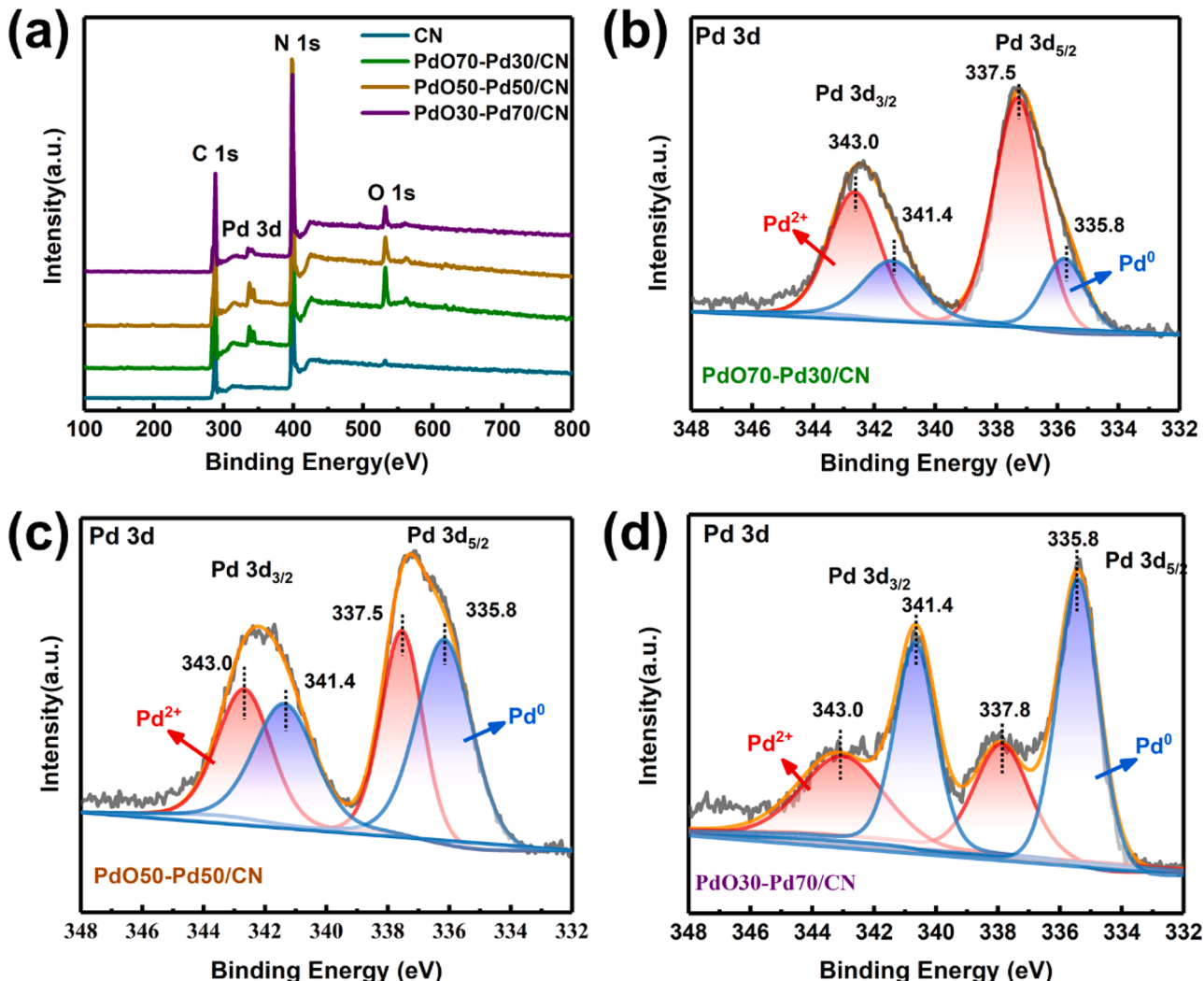


Fig. 2. (a) XPS survey spectrum and Pd 3d high-resolution XPS spectra of (b) PdO70-Pd30/CN, (c) PdO50-Pd50/CN and (d) PdO30-Pd70/CN.

Table 2
Different valence ratios of Pd in samples.

Sample	Before reaction		After reaction	
	Area ratio (Pd ²⁺)	Area ratio (Pd ⁰)	Area ratio (Pd ²⁺)	Area ratio (Pd ⁰)
PdO70-Pd30/ CN	72.1%	27.9%	74.3%	25.7%
PdO50-Pd50/ CN	53.2%	47.8%	50.6%	49.4%
PdO30-Pd70/ CN	29.9%	70.1%	32.1%	68.9%

valence state, XPS tests of CN, PdO70-Pd30/CN, PdO50-Pd50/CN and PdO30-Pd70/CN materials were used. The surface spectra of all materials are shown in Fig. 2(a). On the surface of pure the CN materials, there were only peaks of C, N and a small amount of adsorbed O. When palladium species were introduced, the characteristic peak of palladium species appeared between 300–400 eV and the increase of the peak intensity of O also explained the incorporation of PdO. Fig. S2(a) shows the C 1 s spectra of the CN and PdO-Pd/CN composites. The peak at 288.1 eV belonged to the N-C≡N bond of the sp² hybrid in the nitrogen-containing aromatic ring, which is a typical carbon element peak in carbon nitride. The small peak at 284.6 eV was attributed to carbon impurities on the surface of the material. Further analyzing the N 1 s spectrum in Fig. S2(b), the peaks at 401.2 eV, 400.2 eV and 398.7 eV corresponded to the surface unpolymerized amino group (N-NH₃), N-C₃

and C-N=C in the aromatic ring, respectively [40]. These peaks represented the typical triazine ring structure of g-C₃N₄, which also showed that the chemical states of C and N atoms in the base CN material had no significant change after loading PdO-Pd. Additionally, the peaks at 533.2ev, 531.9ev and 530.8ev in the O 1 s spectrum of Fig. S2(c) belonged to adsorbed oxygen, chemisorbed hydroxyl and lattice oxygen of PdO, respectively. The Pd 3d XPS valence spectra [41] of the PdO-Pd/CN materials were shown in Fig. 2(b)-(d). Among them, the peaks near 343.0 eV and 337.5 eV corresponded to Pd²⁺, and the peaks near 341.4 eV and 335.8 eV belonged to Pd⁰. In the spectrum of Pd70-Pd30/CN, the peak of Pd²⁺ was significantly higher than that of Pd⁰, while the two were close in Pd50-Pd50/CN, and the peak of Pd⁰ was mainly in Pd30-Pd70/CN. At the same time, Table 2 shows that the ratio of the divalent state to the zero state of palladium in PdO70-Pd30/CN, PdO50-Pd50/CN and PdO30-Pd70/CN was close to 70%: 30%, 50%: 50% and 30%: 70%, respectively. The changes in intensity of the lattice oxygen peak in the O 1 s spectrum also verified the changes of palladium valence ratio in the samples. It can be inferred that the three materials were significantly different in the valence ratio of palladium species (PdO-Pd), which proves the successful preparation of cocatalysts with different palladium valence distributions.

The photoelectric properties of the materials were verified by UV-visible diffuse reflectance spectra (UV-Vis DRS) and electrochemical tests. In Fig. 3(a), the CN material had strong absorption in the ultraviolet region and weak absorption in the visible region. When the valence ratio of the Pd cocatalyst changed, their optical spectra in

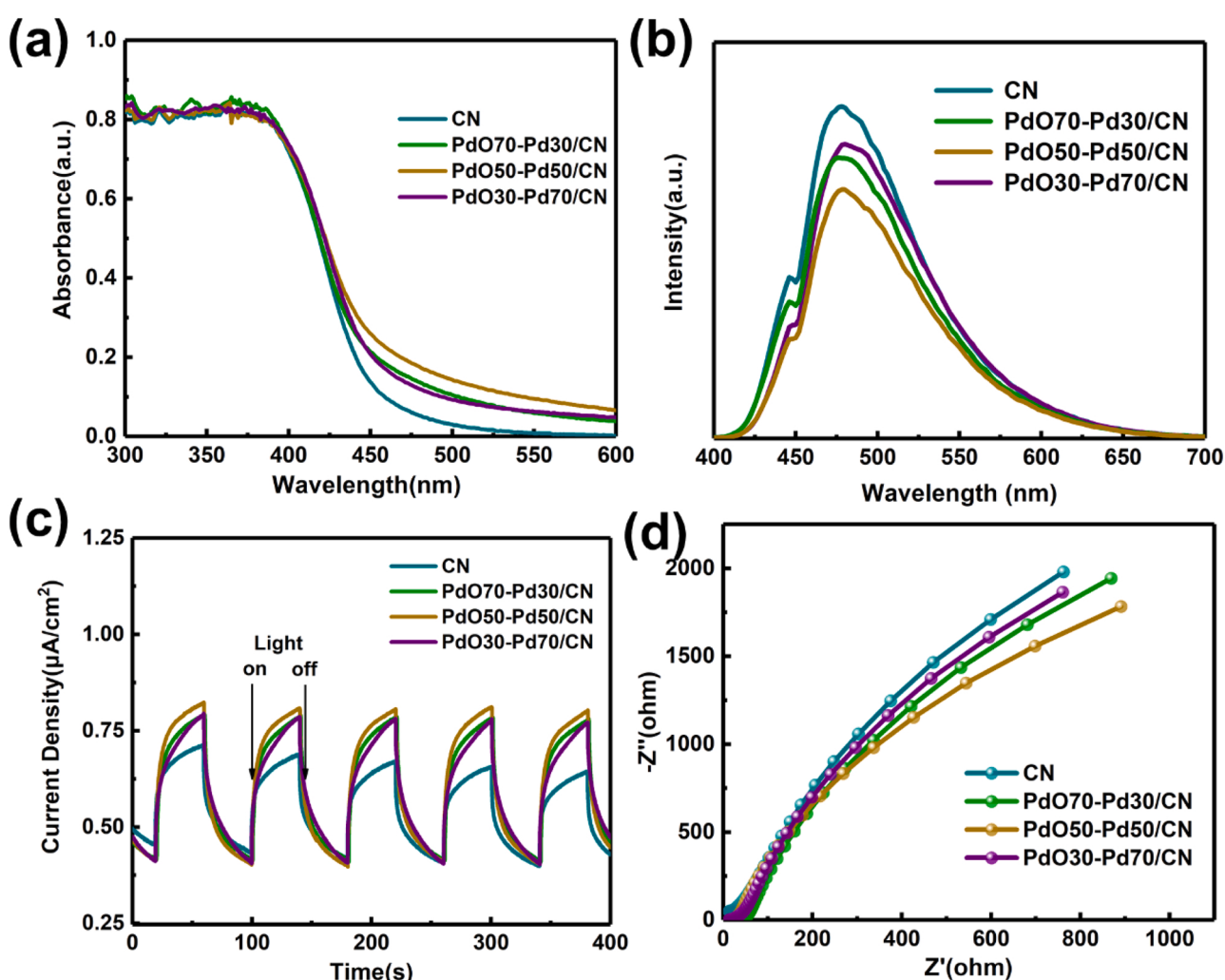


Fig. 3. (a) UV-vis diffuse reflection spectra of samples; (b) PL spectrum; (c) Photocurrent responses; (d) Electrochemical impedance spectra.

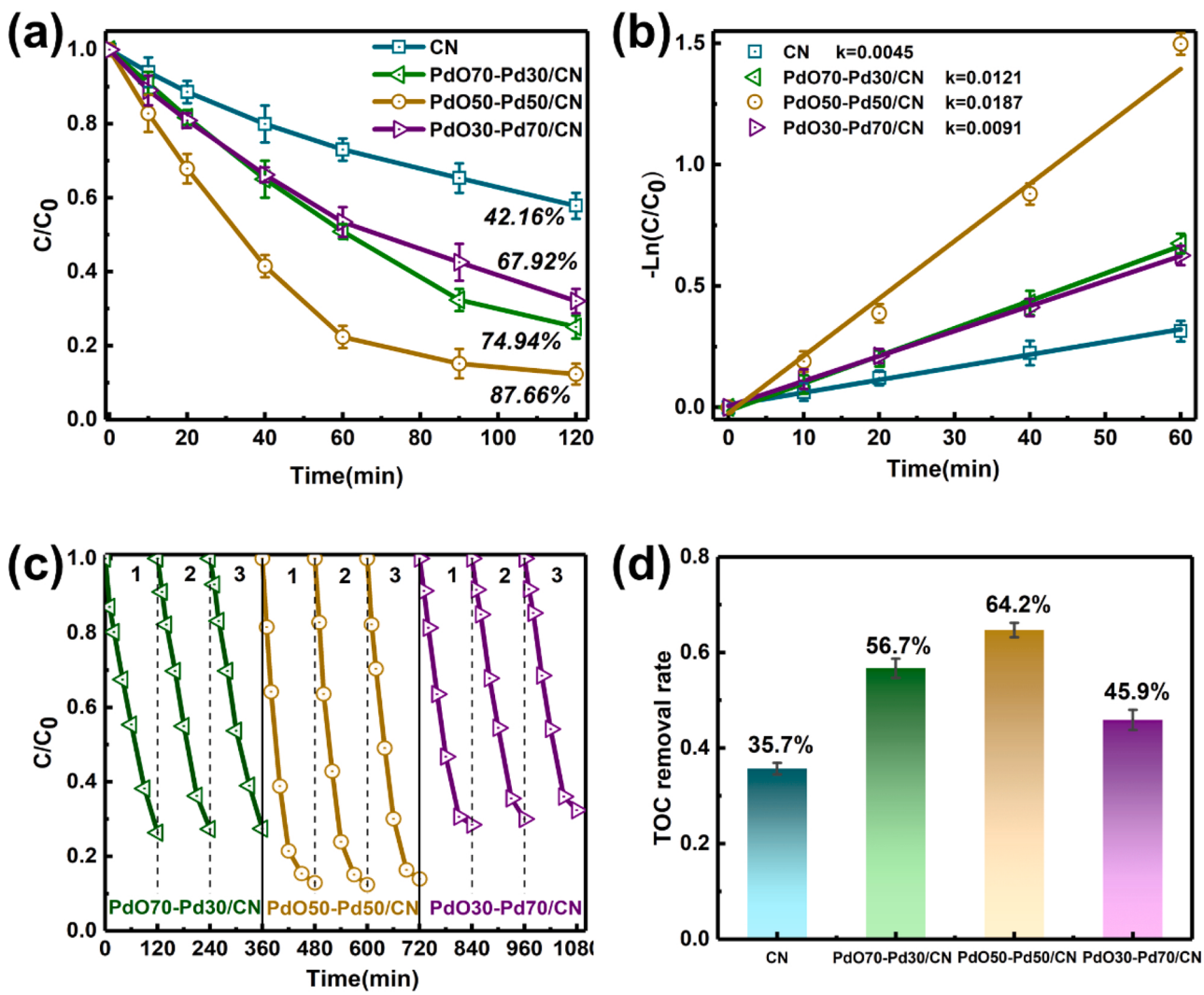


Fig. 4. (a) Photodegradation efficiency, (b) the pseudo-first-order kinetic curves, (c) recyclability and (d) TOC removal rate of samples in the process of sample degradation of CIP solution.

visible-light region resembled to each other, and they did not show an obvious peak indicating the surface plasma resonance phenomenon in those regions. The photogenerated electron and hole separation efficiencies of the CN and Pd cocatalyst materials were studied by PL Spectroscopy, as shown in Fig. 3(b). When the excitation wavelength was 350 nm, all materials had an obvious peak at 476 nm. The peak intensities of the three Pd cocatalysts were lower than that of the pure CN material, but the fluorescence intensity changed little with changes in the ratio of $\text{Pd}^{2+}/(\text{PdO})$ to Pd^0 . The results showed that the addition of palladium cocatalyst inhibited the recombination of photogenerated electrons and holes to a certain extent. It should be noted that the difference in photochemical performance was only a small part of the reason for the difference in the degradation performance of materials PdO70-Pd30/CN, PdO50-Pd50/CN and PdO30-Pd70/CN. The photoelectrochemical test results and electrochemical impedance spectra (EIS) are shown in Fig. 3(c)-(d). It can be seen that the transient photocurrent responses of PdO70-Pd30/CN, PdO50-Pd50/CN and PdO30-Pd70/CN were higher than that of pure CN, but the difference between the three was very small. This trend was consistent with that reflected by EIS.

In addition, the position and width of the bandgap were obtained by UV-DRS and UPS spectra. As shown in Fig. S3 and Fig. S4, the Pd cocatalyst reduced the band gap width to a certain extent, but there was no obvious fluctuation in the band gap with the change in the PdO-Pd

valence ratio. Therefore, it can be inferred that palladium cocatalyst inhibited the recombination of photogenerated electrons and holes to a certain extent, but it was not the main reason for the difference in the photocatalytic degradation of CIP among the three PdO-Pd/CN materials with different valence ratios.

3.2. The relationships between the valence distribution of Pd, active species and photocatalytic performance

After successfully designing and preparing cocatalyst materials with different valence ratios, 10 ppm CIP room temperature aqueous solution was used as an evaluation model for photocatalytic degradation to further explore the influence of palladium cocatalyst valence.

Firstly, 10 mg/L CIP dark adsorption experiment was used to investigate the adsorption performance of palladium cocatalyst materials. Fig. S5(a) shows that the materials basically reached adsorption equilibrium within the first 30 min. Significantly, the adsorption rates of the three materials were very close at the stage of the fastest adsorption (0–15 min). Then, the maximum adsorption capacity experiment was carried out, and the relevant results are shown in Fig. S5(b)&(c). With the increase of CIP concentration, the adsorption capacities of the materials increased linearly, which agreed with the Freundlich isothermal adsorption model [42]. The correlation parameters are shown in Table S1. The value of $1/n$ was opposite to the adsorption capacity, indicating

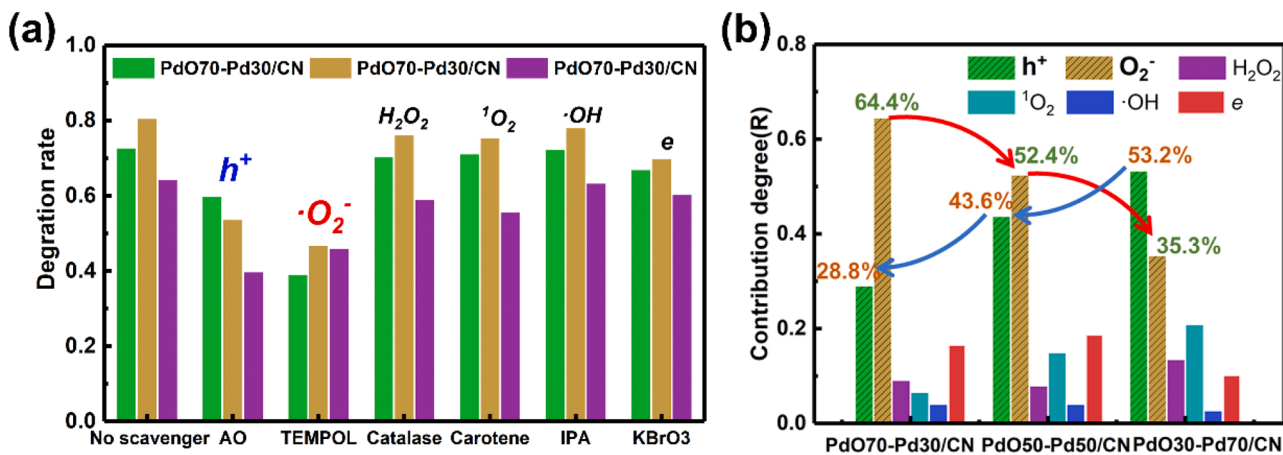


Fig. 5. (a) Effects of scavenger on the photocatalytic degradation efficiency; (b) The contribution of reactive species to the photocatalytic degradation of CIP of PdO-Pd/CN.

the adsorption capacity of several materials for CIP were very close. The BET results shown in Fig. S6 also indicated the specific surface areas of PdO70-Pd30/CN, PdO50-Pd50/CN and PdO30-Pd70/CN are 42.592 m²/g, 43.649 m²/g and 44.547 m²/g respectively, which the difference between them could be ignored(<2 m²/g).

Then, in the degradation experiment, the photodegradation efficiency (η) can be calculated by the Eq. (1) [43–45]:

$$\eta = \frac{(C_0 - C_t)}{C_0} \times 100\% \quad (1)$$

The reaction rate constant of photocatalytic degradation of CIP solution can be determined by using Eq. (2):

$$k_1 = -\ln\left(\frac{C_t}{C_0}\right) \quad (2)$$

where C_0 , C_t were the initial concentration (mg/L) and concentration (mg/L) at time t of CIP solution, t is the degradation time and k is the reaction rate constant.

Fig. 4(a) shows the time profile curves for photocatalytic degradation of 10 ppm CIP solution when using Pd cocatalyst samples, and the pristine g-C₃N₄ (CN) was used as the reference without palladium species. Obviously, after the introduction of palladium cocatalyst, the degradation performance of the material was improved to varying degrees, with the change in the PdO-Pd valence ratio. PdO50-Pd50/CN displayed degradation of 87.7% CIP solution in 120 min, higher than 74.9% of PdO70-Pd30/CN, 67.9% of PdO30-Pd70/CN and 42.6% of pure CN. The change processes of absorbance at 279 nm with illumination time are shown in Fig. S7(a)–(c). The peak intensity decreased gradually with time, and the peak with the highest intensity shifted gradually, which was caused by the degradation of CIP into other small molecules. The degradation performances of several materials conform to the pseudo first-order kinetics. As shown in Fig. 4(b), the kinetic curves have good linearity. PdO50-Pd50/CN had the highest average k_1 value of 0.0187, and the average k_1 values of PdO70-Pd30/CN and PdO30-Pd70/CN were 0.0121 and 0.0091, respectively, which were higher than that of pure CN (0.0045). This result indicated that the degradation efficiency and degradation rate of the three materials were different. In addition, TOC was used to further explore the mineralization efficiency of CIP in the photocatalytic process (Fig. 4(c)). After 120 min of illumination, the TOC removal rates of PdO70-Pd30/CN, PdO50-Pd50/CN and PdO30-Pd70/CN were 56.7%, 64.2% and 45.9%, respectively, which were higher than that of CN (35.7%). Significantly, the difference in the TOC removal rate was consistent with the degradation effect. Furthermore, in order to test the recovery stability of the samples, the PdO-Pd/CN materials were tested for three cycles (Fig. 4

(d)) without significant performance degradation. In addition, we compared the valence ratio of Pd in the materials before and after the degradation reaction. The results showed that the ratios of Pd²⁺/Pd⁰ only slightly changed (Fig. S8 and Table 2). Specifically, the ratio of Pd²⁺/Pd⁰ of PdO70-Pd30/CN changed from 72.1%/27.9–74.3%/25.7%; that of PdO50-Pd50/CN changed from 53.2%/47.8–50.6%/49.4%; while that of PdO30-Pd70/CN changed from 29.9%/70.1–32.1%/68.9%. These results show that PdO-Pd/CN materials are still stable under photocatalytic conditions.

In order to further analyze the causes of degradation differences, capture experiments were used to discuss the contribution of active species O₂⁻, h⁺, H₂O₂, ^1O₂, ·OH and e captured by TEMPOL, AO, CAT, carotene, IPA and KBrO₃, respectively, in the process of photocatalytic degradation of 10 ppm CIP solution for samples. As shown in Fig. 5(a), the addition of scavenger had obvious inhibitory effect on photocatalytic activity, and the highest inhibitory effects were TEMPOL and AO. It can be inferred that O₂⁻ and h⁺ were the main active species in the photocatalytic degradation of CIP of the three PdO-Pd/CN materials.

Furthermore, we fitted the pseudo-zero-order, pseudo-first-order and pseudo-second-order kinetic models (Eqs. (3)–(5)) [46,47] for the degradation reaction in the presence of scavengers, to verify whether it conforms to the first-order kinetic process and uses the rate constant (k_1) to calculate the contribution (Eqs. (6)–(11) [48–50]).

$$C_t - C_0 = k_0 \times t \quad (3)$$

$$\ln\left(\frac{C_0}{C_t}\right) = k_1 \times t \quad (4)$$

$$\frac{1}{C_t} - \frac{1}{C_0} = k_2 \times t \quad (5)$$

where C_0 and C_t were the initial concentration (mg/L) and concentration (mg/L) at time t of CIP solution. k_0 , k_1 and k_2 were the apparent zero-order kinetic rate constant (mg/L), first-order kinetic rate constant (min⁻¹) and second-order kinetic rate constant (L/mg/min), respectively.

The fitted kinetic curves and the corresponding calculated kinetic constants are shown in Fig. S9–S11 and Table S2–S4 the revised manuscript. By comparing the correlation coefficient (R^2), it seems that the pseudo first-order kinetic model is more suitable for CIP degradation process here in the presence of scavengers. Specifically, the correlation coefficients of first-order fitting are all larger than 0.99, while most of the correlation coefficients for zero-order and second-order fitting are less than 0.96 (some are even less than 0.90). On this basis, all degradation reactions referred in this paper should follow the pseudo-first-order, so the method of using the rate constant(k_1) to calculate the contribution is

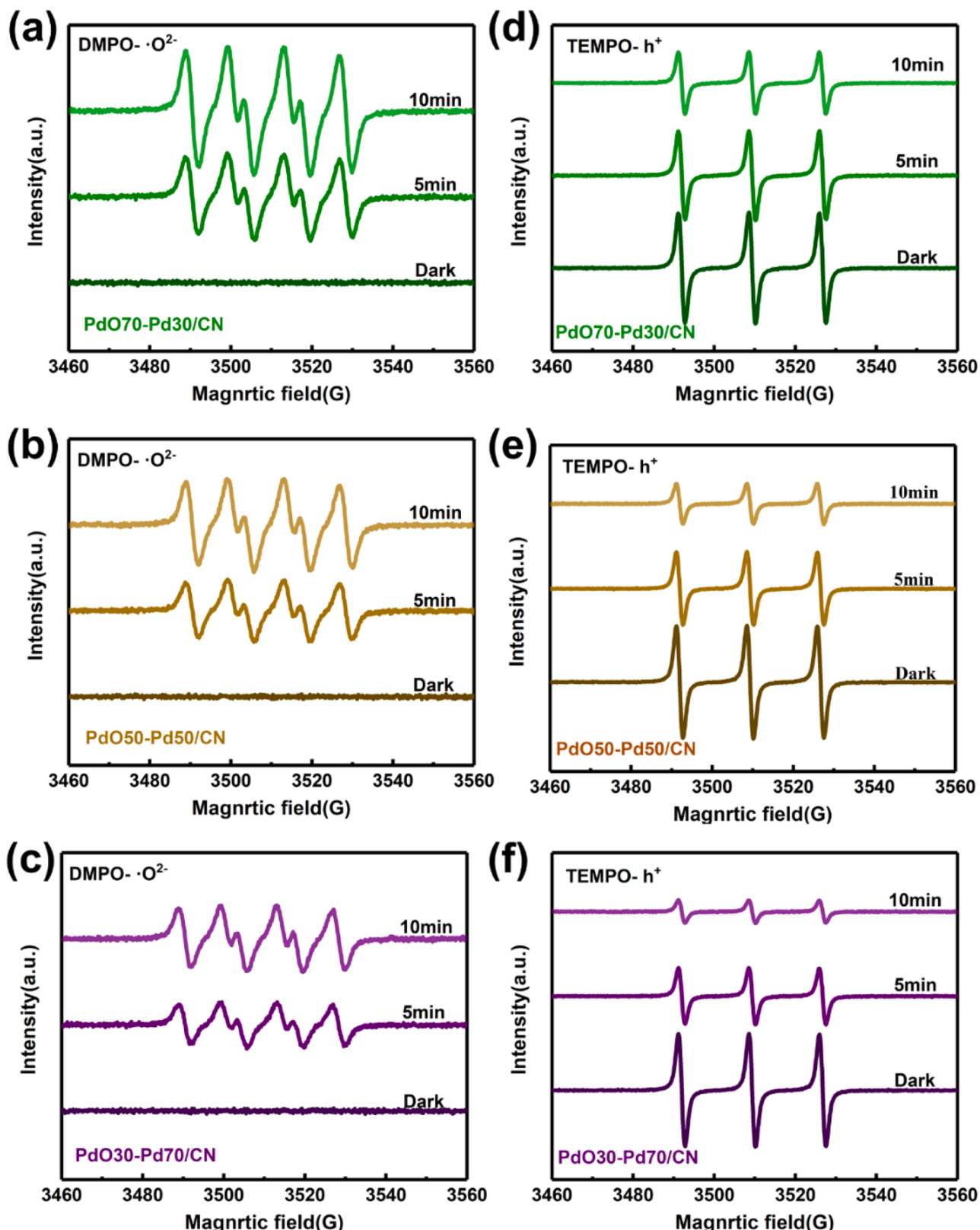


Fig. 6. ESR spectra of $\cdot\text{O}_2^-$ of (a) PdO70-Pd30/CN, (b) PdO50-Pd50/CN, (c) PdO30-Pd70/CN and h^+ of (d) PdO70-Pd30/CN, (e) PdO50-Pd50/CN, and (f) PdO30-Pd70/CN in the dark and under visible light irradiation.

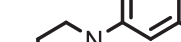
Table 3

Mass spectrometry piece information and proposed structure of photocatalytic products in the catalytic degradation of CIP by PdO-Pd/CN materials.

Intermediate Products	Retention Time (min)	ESI (+) MS (<i>m/z</i>)	Molecular Formula	Supposed Structural Formula
CIP	2.58–2.68	332	C ₁₇ H ₁₈ FN ₃ O ₃	
P1	3.70–3.81	362	C ₁₇ H ₁₆ FN ₃ O ₅	
P2	2.10–2.23	334	C ₁₆ H ₁₆ FN ₃ O ₄	
P3	4.77–4.87	291	C ₁₄ H ₁₁ FN ₂ O ₄	
P4	6.11–6.33	316	C ₁₆ H ₁₆ N ₃ O ₄	
P5	6.03–6.10	245	C ₁₃ H ₁₃ N ₂ O ₃	
P6	1.60–1.72	348	C ₁₇ H ₁₈ FN ₃ O ₄	

(continued on next page)

Table 3 (*continued*)

Intermediate Products	Retention Time (min)	ESI (+) MS (<i>m/z</i>)	Molecular Formula	Supposed Structural Formula
P7	6.42–6.50	313	C ₁₇ H ₁₈ N ₃ O ₃	
P8	4.45–4.54-	217	C ₁₂ H ₁₂ N ₂ O ₂	

relatively reasonable. Accordingly, we used Eqs. (6)–(11), and the first-order rate constant (k_1) to calculate the contribution of each active species.

$$R_{O_2^-} = \frac{K_{O_2^-}}{K} = \frac{K - K_{TEMPOL}}{K} \quad (6)$$

$$R_{H_2O_2} = \frac{K_{H_2O_2}}{K} = \frac{K - K_{CAT}}{K} \quad (7)$$

$$R_{1o_2} = \frac{K_{1o_2}}{K} = \frac{K - K_{carotene}}{K} \quad (8)$$

$$R_{1_{O_2}} = \frac{K_{1_{O_2}}}{K} = \frac{K - K_{carotene}}{K} \quad (9)$$

$$R_{OH} = \frac{K_{OH}}{K} = \frac{K - K_{IPA}}{K} \quad (10)$$

$$R_e = \frac{K_e}{K} = \frac{K - K_{KBrO_3}}{K} \quad (11)$$

where R is the fractional contribution of the reactive species to the reaction rate constant k in the absence of quenching agents. k_i is the first-order kinetic reaction rate constant of O_2^- , h^+ , H_2O_2 , ${}^1\text{O}_2$, OH and e and in the presence of TEMPOL, ammonium oxalate (AO), CAT, carotene, isopropanol (IPA) and KBrO_3 , respectively.

The results are shown in Fig. 5(b). In sample PdO70-Pd30/CN, the contribution of O_2^- was higher than h^+ , it was basically close in sample PdO50-Pd50/CN, and in sample PdO30-Pd70/CN, the contribution of h^+ was higher than that of O_2^- . With the changes in the proportion of Pd^{2+} (PdO) and Pd^0 in palladium species in the samples (PdO: 70%→50%→30%, Pd: 30%→50%→70%), the contribution of O_2^- and h^+ in the degradation process also changed correspondingly (O_2^- : 64.4%→52.4%→35.7%, h^+ : 28.8%→43.6%→53.2%). Therefore, we concluded that in the PdO-Pd/CN material system, the ratio of PdO to Pd affected

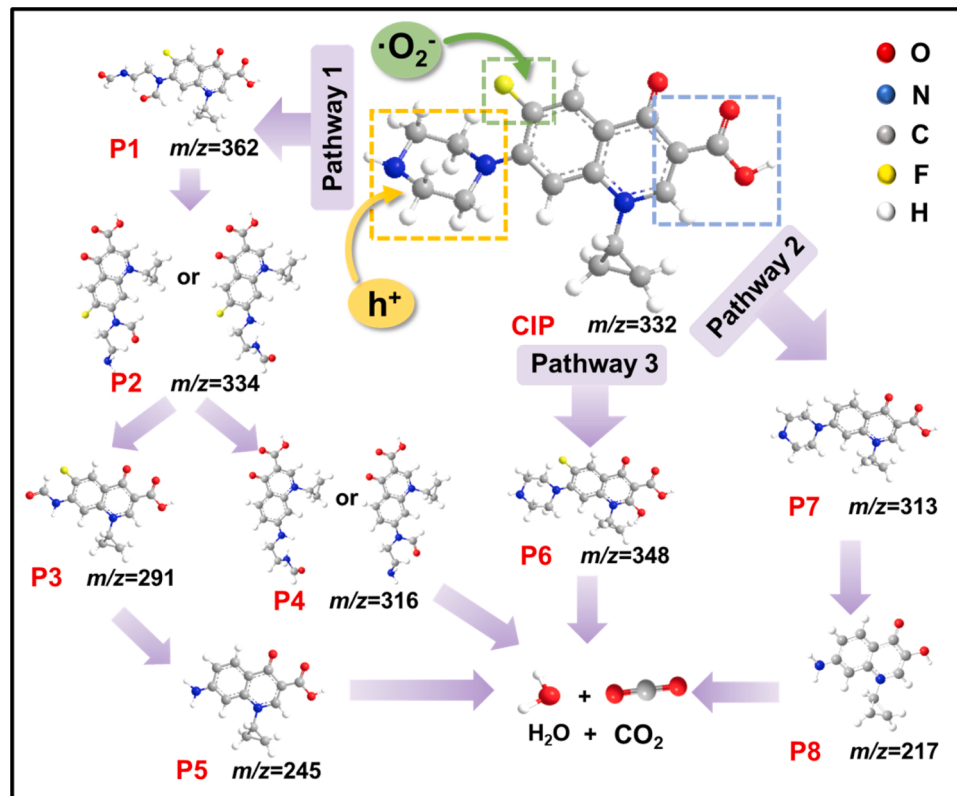


Fig. 7. Possible CIP photodegradation pathway over the PdO-Pd/CN samples under visible light irradiation.

the contribution of $\cdot\text{O}_2^-$ and h^+ to the degradation process of CIP.

At the same time, the ESR results (Fig. 6) showed that the concentration of $\cdot\text{O}_2^-$ was $\text{PdO70-Pd30/CN} > \text{PdO50-Pd50/CN} > \text{PdO30-Pd70/CN}$, and the concentration of photogenerated holes was $\text{PdO30-Pd70/CN} > \text{PdO50-Pd50/CN} > \text{PdO70-Pd30/CN}$, which was consistent with the conclusion of the capture experiment. Specifically, the generated oxidative active species are highly related to the distribution of valence of Pd. When $\text{Pd}^{2+}(\text{PdO})$ dominated the cocatalyst, $\cdot\text{O}_2^-$ was the main active species. In the Pd^0 dominated cocatalyst, h^+ became the main active species. Interestingly, when $\text{Pd}^{2+}(\text{PdO})$ and Pd^0 were equal to each other, the contribution of $\cdot\text{O}_2^-$ was also close to that of h^+ . In addition, the capture experiment was carried out using pure $\text{g-C}_3\text{N}_4$ without Pd as the control. The results are shown in Fig. S12, that the main active species of pure $\text{g-C}_3\text{N}_4$ in the CIP photocatalytic degradation system are $\cdot\text{O}_2^-$ and h^+ , which is related to the combined attack effect of $\cdot\text{O}_2^-$ and h^+ on CIP.

3.3. The working mechanism of the Pd based cocatalyst and the degradation pathway of CIP

The main photocatalytic degradation intermediates of CIP were determined by LC-MS. Table 3 shows the mass spectrum information and structural formulas of possible intermediates. Possible degradation pathways are summarized in Fig. 7.

In the **pathway 1**, $\cdot\text{O}_2^-$ and h^+ attacked the piperazinyl group, resulting in the oxidation of CIP (m/z 332) to form P1 (m/z 362). Next, h^+ attacked the N-C bond of the opened piperazine ring to form P2 (m/z 334). Then, under the further attack of h^+ , P2 successively generated P3 (m/z 291) and P5 (m/z 245); on the other hand, P2 will also generate P4 (m/z 316) and further decompose under the action of $\cdot\text{O}_2^-$. Finally, the piperazinyl substituent was completely destroyed, and the intermediate was further degraded into other small molecules and mineralized to form H_2O and CO_2 . In the **pathway 2**, the CIP molecule was defluorinated and oxidized. First, the attack of $\cdot\text{O}_2^-$ triggers the substitution of hydroxyl groups to F and further oxidizes and breaks the piperazine ring to form P7 (m/z 313). Then, further hydrolysis and oxidation will destroy piperazine ring and carboxyl groups, P7 occurred oxidative decarboxylation to form P8 (m/z 217) and continued to decompose into water and carbon dioxide. In the **pathway 3**, $\cdot\text{OH}$ attacked the quinolone ring and generated P6 (m/z 348) through addition reaction, however, no further intermediates were detected, indicating that this pathway is not the main pathway. In general, $\cdot\text{O}_2^-$ and h^+ were essential initiators and leaders in the main pathway of CIP degradation. With the change of contribution degree of $\cdot\text{O}_2^-$ and h^+ , the rate and degree of degradation will bound to change due to the process change of pathway [51,52].

In addition, Fig. S13 and Table. S5 showed the crucial intermediates and degradation pathways of CIP using pristine $\text{g-C}_3\text{N}_4$ were basically the same as that using Pd cocatalyst promoted samples. This is because the active species of CIP degradation with pristine $\text{g-C}_3\text{N}_4$ are also $\cdot\text{O}_2^-$ and h^+ , which contribution ratios are 32.1% and 41.2%, respectively (Fig. S12). Besides, it should be noted that two intermediates (P7 $m/z = 217$, P5 $m/z = 245$) were missed in the result of LC-MS test of $\text{g-C}_3\text{N}_4$. But at the same time, we detected some other small intermediates (P9 $m/z = 283$, P10 $m/z = 274$). This indicated that there were possibly some different degradation pathways using pristine $\text{g-C}_3\text{N}_4$ when the intermediates were smaller than $m/z = 300$ [1,2].

According to the results of active species capture and ESR, we infer that the valence state of the palladium based cocatalyst on carbon nitride will affect the contribution of $\cdot\text{O}_2^-$ and h^+ in CIP photocatalytic degradation, further affecting its dominant degradation process, and thus affecting the degradation rate and TOC removal rate.

Specifically, when $\text{Pd}^{2+}(\text{PdO})$ accounts for the main body of the cocatalyst, the active species are mainly $\cdot\text{O}_2^-$, and when Pd^0 accounts for the main body of the cocatalyst, the active species are mainly h^+ . Further, the differential charge diagram in Fig. 8 shows that both $\text{Pd}^{2+}(\text{PdO})$ and Pd^0 cluster sites can accumulate electrons, in which the

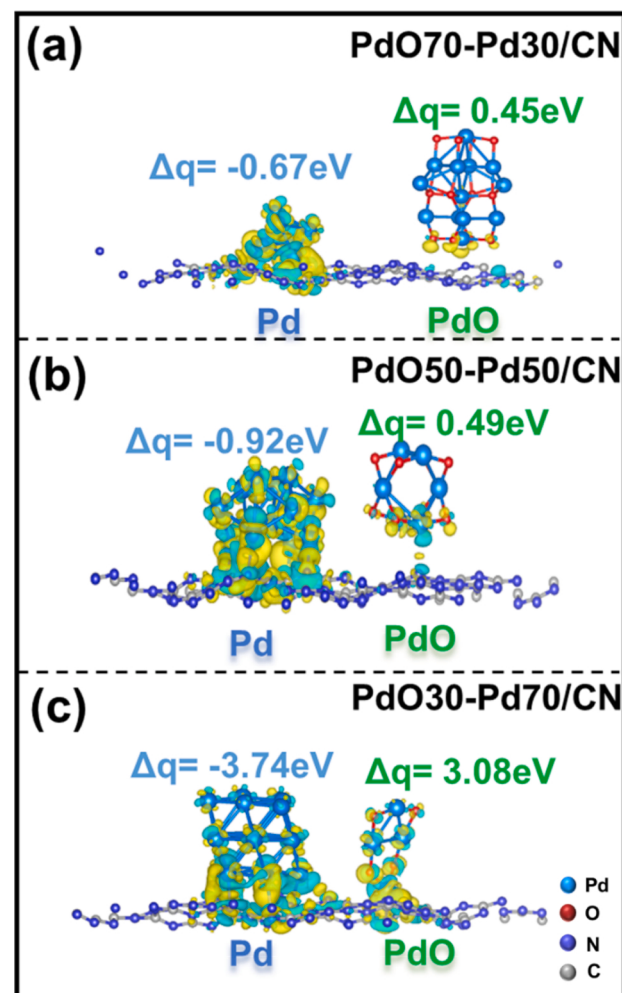


Fig. 8. Differential charge diagram and Bader charge of (a) PdO70-Pd30/CN , (b) PdO50-Pd50/CN and (c) PdO30-Pd70/CN .

yellow part represents the electron enrichment region (positive charge) and the green part represents the electron consumption region (negative charge). At the same time, the Bader charges of the samples were calculated, in which Δq on Pd clusters were: -0.67 eV , -0.92 eV , -3.74 eV ; Δq on PdO clusters were: 0.45 eV , 0.49 eV , 3.08 eV . Therefore, we infer that those electrons tend to cluster on PdO clusters to further form ROS species. In addition, the adsorption energy relationship (Fig. S14 & Table. S6) calculated by the O_2 adsorption model was: $E_{\text{ads}}(\text{PdO70-Pd30/CN}) > E_{\text{ads}}(\text{PdO50-Pd50/CN}) > E_{\text{ads}}(\text{PdO30-Pd70/CN})$. Therefore, PdO sites were more likely to produce more active $\cdot\text{O}_2^-$. In contrast, when the proportion of PdO decreased ($\text{PdO70-Pd30/CN} \rightarrow \text{Pd30-Pd70/CN}$), the concentration of $\cdot\text{O}_2^-$ produced was not high enough, which caused h^+ become the dominant active species in the competition. From the pathway inference, it can be seen that the photocatalytic degradation process of CIP was a combined process of $\cdot\text{O}_2^-$ and h^+ . Therefore, when the PdO-Pd ratio was in a delicate balance (PdO50-Pd50/CN), $\cdot\text{O}_2^-$ and h^+ coordination produced the best degradation effect.

4. Conclusion

In this work, as an example of photocatalysis, we designed simple wet chemical methods to load palladium cocatalysts with different valence distributions (PdO70-Pd30/CN , PdO70-Pd30/CN and PdO70-Pd30/CN) on $\text{g-C}_3\text{N}_4$ nanosheets. TEM, ICP, XPS, XRD and FTIR results showed that palladium cocatalysts with different valence

distributions were successfully supported on carbon nitride matrix with close loading (~ 1 wt%) and uniform particle size ($2 \sim 3$ nm). The UV Vis DRS, PL and EIS results showed that the photoelectric properties of the PdO-Pd/CN materials were only slightly different. Taking the photocatalytic degradation of ciprofloxacin as the evaluation model, we found that the different ratios of $\text{Pd}^{2+}/\text{Pd}^0$ caused variations in the O_2^- and h^+ contributions to the degradation of CIP, which in turn led to differences in degradation performance and TOC removal rate over the same irradiation time. When Pd^{2+} (PdO) dominated the cocatalyst, O_2^- was the main active species. While in Pd^0 dominated cocatalyst, h^+ became the main active species. Interestingly, when Pd^{2+} (PdO) and Pd^0 were equal to each other, the contribution of O_2^- was also close to that of h^+ . Then, the theoretical simulations revealed that surface states e.g., electron distribution and the adsorption ability of O_2 on different Pd species determined the production of O_2^- and h^+ . Among them, PdO50-Pd50/CN showed the best performance for degrading ciprofloxacin, and the degradation process of ciprofloxacin was caused by the combined attack of O_2^- and h^+ .

CRediT authorship contribution statement

Fa Guo: Formal analysis, Writing – original draft. **Hao Zhang:** Investigation, Formal analysis, Resources. **Hui Li:** Investigation, Formal analysis, Software. **Zhurui Shen:** Conceptualization, Methodology, Supervision.

Declaration of Competing Interest

The authors declare that they have no known competing financial interests or personal relationships that could have appeared to influence the work reported in this paper.

Acknowledgements

This work was supported by the grants from the Fundamental Research Funds for the Central Universities, Nankai University (ZB19100141), the National Natural Science Foundation of China (21872102 and 22172080) and the Tianjin “Project + Team” innovation team, 2020.

Appendix A. Supporting information

Supplementary data associated with this article can be found in the online version at [doi:10.1016/j.apcatb.2022.121092](https://doi.org/10.1016/j.apcatb.2022.121092).

References

- [1] X. Meng, L. Liu, S. Ouyang, H. Xu, D. Wang, N. Zhao, J. Ye, Nanometals for solar-to-chemical energy conversion: from semiconductor-based photocatalysis to plasmon-mediated photocatalysis and photo-thermocatalysis, *Adv. Mater.* 28 (2016) 6781–6803.
- [2] C. Xia, T. Hong Chuong Nguyen, X. Cuong Nguyen, S. Young Kim, D.L.T. Nguyen, P. Raizada, P. Singh, V.-H. Nguyen, C. Chien Nguyen, V. Chinh Hoang, Q. Van Le, Emerging cocatalysts in TiO_2 -based photocatalysts for light-driven catalytic hydrogen evolution: progress and perspectives, *Fuel* 307 (2022).
- [3] V. Soni, C. Xia, C.K. Cheng, V.-H. Nguyen, D.L.T. Nguyen, A. Bajpai, S.Y. Kim, Q. V. Le, A.A.P. Khan, P. Singh, P. Raizada, Advances and recent trends in cobalt-based cocatalysts for solar-to-fuel conversion, *Appl. Mater. Today* 24 (2021).
- [4] G. Zhao, X. Xu, Cocatalysts from types, preparation to applications in the field of photocatalysis, *Nanoscale* 13 (2021) 10649–10667.
- [5] R. Li, W. Zhang, K. Zhou, Metal-organic-framework-based catalysts for photoreduction of CO_2 , *Adv. Mater.* 30 (2018), e1705512.
- [6] Y. Yu, X. Dong, P. Chen, Q. Geng, H. Wang, J. Li, Y. Zhou, F. Dong, Synergistic effect of Cu single atoms and Au-Cu alloy nanoparticles on TiO_2 for efficient CO_2 photoreduction, *ACS Nano* 15 (2021) 14453–14464.
- [7] J. Ran, M. Jaroniec, S.Z. Qiao, Cocatalysts in semiconductor-based photocatalytic CO_2 reduction: achievements, challenges, and opportunities, *Adv. Mater.* 30 (2018).
- [8] Y.-N. Gong, J.-H. Mei, J.-W. Liu, H.-H. Huang, J.-H. Zhang, X. Li, D.-C. Zhong, T.-B. Lu, Manipulating metal oxidation state over ultrastable metal-organic frameworks for boosting photocatalysis, *Appl. Catal. B Environ.* 292 (2021).
- [9] A. Meng, L. Zhang, B. Cheng, J. Yu, Dual cocatalysts in TiO_2 photocatalysis, *Adv. Mater.* 31 (2019), e1807660.
- [10] X.N. Ren, Z.Y. Hu, J. Jin, L. Wu, C. Wang, J. Liu, F. Liu, M. Wu, Y. Li, G. V. Tendeloo, B.L. Su, Cocatalyzing Pt/PtO phase-junction nanodots on hierarchically porous TiO_2 for highly enhanced photocatalytic hydrogen production, *ACS Appl. Mater. Interfaces* 9 (2017) 29687–29698.
- [11] S. Chen, S. Li, R. You, Z. Guo, F. Wang, G. Li, W. Yuan, B. Zhu, Y. Gao, Z. Zhang, H. Yang, Y. Wang, Elucidation of active sites for CH_4 catalytic oxidation over Pd/ CeO_2 via tailoring metal-support interactions, *ACS Catal.* 11 (2021) 5666–5677.
- [12] J. Lv, S. Wu, Z. Tian, Y. Ye, J. Liu, C. Liang, Construction of PdO-Pd interfaces assisted by laser irradiation for enhanced electrocatalytic N_2 reduction reaction, *J. Mater. Chem. A* 7 (2019) 12627–12634.
- [13] W.J. Ong, L.L. Tan, Y.H. Ng, S.T. Yong, S.P. Chai, Graphitic carbon nitride ($\text{g-C}_3\text{N}_4$)-based photocatalysts for artificial photosynthesis and environmental remediation: are we a step closer to achieving sustainability? *Chem. Rev.* 116 (2016) 7159–7329.
- [14] P. Chen, L. Blaney, G. Cagnetta, J. Huang, B. Wang, Y. Wang, S. Deng, G. Yu, Degradation of ofloxacin by perylene diimide supramolecular nanofiber sunlight-driven photocatalysis, *Environ. Sci. Technol.* 53 (2019) 1564–1575.
- [15] D. Fatta-Kassinos, M.I. Vasquez, K. Kummerer, Transformation products of pharmaceuticals in surface waters and wastewater formed during photolysis and advanced oxidation processes-degradation, elucidation of byproducts and assessment of their biological potency, *Chemosphere* 85 (2011) 693–709.
- [16] R. Gothwal, T. Shashidhar, Antibiotic pollution in the environment: a review, *CLEAN - Soil, Air, Water* 43 (2015) 479–489.
- [17] P. Kovalakova, L. Cizmas, T.J. McDonald, B. Marsalek, M. Feng, V.K. Sharma, Occurrence and toxicity of antibiotics in the aquatic environment: a review, *Chemosphere* 251 (2020), 126351.
- [18] S. Li, T. Huang, P. Du, W. Liu, J. Hu, Photocatalytic transformation fate and toxicity of ciprofloxacin related to dissociation species: Experimental and theoretical evidences, *Water Res.* 185 (2020), 116286.
- [19] I. Michael, L. Rizzo, C.S. McArdell, C.M. Manaia, C. Merlin, T. Schwartz, C. Dagot, D. Fatta-Kassinos, Urban wastewater treatment plants as hotspots for the release of antibiotics in the environment: a review, *Water Res.* 47 (2013) 957–995.
- [20] F. Wang, Y. Feng, P. Chen, Y. Wang, Y. Su, Q. Zhang, Y. Zeng, Z. Xie, H. Liu, Y. Liu, W. Lv, G. Liu, Photocatalytic degradation of fluoroquinolone antibiotics using ordered mesoporous $\text{g-C}_3\text{N}_4$ under simulated sunlight irradiation: kinetics, mechanism, and antibacterial activity elimination, *Appl. Catal. B Environ.* 227 (2018) 114–122.
- [21] F. Mansouri, K. Chouchene, N. Roche, M. Ksibi, Removal of pharmaceuticals from water by adsorption and advanced oxidation processes: state of the art and trends, *Appl. Sci.* 11 (2021).
- [22] Z. Xiong, H. Zhang, W. Zhang, B. Lai, G. Yao, Removal of nitrophenols and their derivatives by chemical redox: a review, *Chem. Eng. J.* 359 (2019) 13–31.
- [23] H.R. Ghatak, Advanced oxidation processes for the treatment of biorecalcitrant organics in wastewater, *Crit. Rev. Environ. Sci. Technol.* 44 (2014) 1167–1219.
- [24] T. An, H. Yang, G. Li, W. Song, W.J. Cooper, X. Nie, Kinetics and mechanism of advanced oxidation processes (AOPs) in degradation of ciprofloxacin in water, *Appl. Catal. B Environ.* 94 (2010) 288–294.
- [25] M. Cohá, G. Farinelli, A. Tiraferri, M. Minella, D. Vione, Advanced oxidation processes in the removal of organic substances from produced water: potential, configurations, and research needs, *Chem. Eng. J.* 414 (2021).
- [26] A. Kubacka, M. Fernandez-Garcia, G. Colon, Advanced nanoarchitectures for solar photocatalytic applications, *Chem. Rev.* 112 (2012) 1555–1614.
- [27] Y. Nosaka, A.Y. Nosaka, Generation and detection of reactive oxygen species in photocatalysis, *Chem. Rev.* 117 (2017) 11302–11336.
- [28] L. Luo, T. Zhang, M. Wang, R. Yun, X. Xiang, Recent advances in heterogeneous photo-driven oxidation of organic molecules by reactive oxygen species, *ChemSusChem* 13 (2020) 5173–5184.
- [29] Z. Long, Q. Li, T. Wei, G. Zhang, Z. Ren, Historical development and prospects of photocatalysts for pollutant removal in water, *J. Hazard Mater.* 395 (2020), 122599.
- [30] J. Xiao, Q. Han, Y. Xie, J. Yang, Q. Su, Y. Chen, H. Cao, Is C_3N_4 chemically stable toward reactive oxygen species in sunlight-driven water treatment, *Environ. Sci. Technol.* 51 (2017) 13380–13387.
- [31] H. Shang, S. Huang, H. Li, M. Li, S. Zhao, J. Wang, Z. Ai, L. Zhang, Dual-site activation enhanced photocatalytic removal of no with Au/ CeO_2 , *Chem. Eng. J.* 386 (2020).
- [32] W. Liu, Y. Li, F. Liu, W. Jiang, D. Zhang, J. Liang, Visible-light-driven photocatalytic degradation of diclofenac by carbon quantum dots modified porous $\text{g-C}_3\text{N}_4$: mechanisms, degradation pathway and DFT calculation, *Water Res* 150 (2019) 431–441.
- [33] Y. Mu, G. Zhan, C. Huang, X. Wang, Z. Ai, J. Zou, S. Luo, L. Zhang, Dechlorination-hydroxylation of atrazine to hydroxyatrazine with thiosulfate: a detoxification strategy in seconds, *Environ. Sci. Technol.* 53 (2019) 3208–3216.
- [34] S. Cao, J. Low, J. Yu, M. Jaroniec, Polymeric photocatalysts based on graphitic carbon nitride, *Adv. Mater.* 27 (2015) 2150–2176.
- [35] X. Li, B. Kang, F. Dong, Z. Zhang, X. Luo, L. Han, J. Huang, Z. Feng, Z. Chen, J. Xu, B. Peng, Z.L. Wang, Enhanced photocatalytic degradation and $\text{H}_2/\text{H}_2\text{O}_2$ production performance of S-pCN/WO₂.72 S-scheme heterojunction with appropriate surface oxygen vacancies, *Nano Energy* 81 (2021).
- [36] F. Chen, Q. Yang, X. Li, G. Zeng, D. Wang, C. Niu, J. Zhao, H. An, T. Xie, Y. Deng, Hierarchical assembly of graphene-bridged Ag₃Po₄/Ag/BiVO₄ (040) Z-scheme photocatalyst: an efficient, sustainable and heterogeneous catalyst with enhanced visible-light photoactivity towards tetracycline degradation under visible light irradiation, *Appl. Catal. B Environ.* 200 (2017) 330–342.

- [37] Y. Li, S. Ouyang, H. Xu, X. Wang, Y. Bi, Y. Zhang, J. Ye, Constructing solid-gas-interfacial fenton reaction over alkalinized-C₃N₄ photocatalyst to achieve apparent quantum yield of 49% at 420 nm, *J. Am. Chem. Soc.* 138 (2016) 13289–13297.
- [38] N. Wang, J. Wang, J. Hu, X. Lu, J. Sun, F. Shi, Z.-H. Liu, Z. Lei, R. Jiang, Design of palladium-doped g-C₃N₄ for enhanced photocatalytic activity toward hydrogen evolution reaction, *ACS Appl. Energy Mater.* 1 (2018) 2866–2873.
- [39] H. Xu, J. Yan, Y. Xu, Y. Song, H. Li, J. Xia, C. Huang, H. Wan, Novel visible-light-driven AgX/graphite-like C₃N₄ (X=Br, I) hybrid materials with synergistic photocatalytic activity, *Appl. Catal. B Environ.* 129 (2013) 182–193.
- [40] M. Lei, Z. Wang, L. Zhu, W. Nie, H. Tang, Complete debromination of 2,2',4,4'-tetrabromodiphenyl ether by visible-light photocatalysis on g-C₃N₄ supported Pd, *Appl. Catal. B Environ.* 261 (2020).
- [41] Z. Yin, M. Han, Z. Hu, L. Feng, Y. Liu, Z. Du, L. Zhang, Peroxymonosulfate enhancing visible light photocatalytic degradation of bezafibrate by Pd/g-C₃N₄ catalysts: the role of sulfate radicals and hydroxyl radicals, *Chem. Eng. J.* 390 (2020).
- [42] Z. Wei, Y. Liu, J. Wang, R. Zong, W. Yao, J. Wang, Y. Zhu, Controlled synthesis of a highly dispersed BiPO₄ photocatalyst with surface oxygen vacancies, *Nanoscale* 7 (2015) 13943–13950.
- [43] J. Liu, Y. Yue, W. Wang, F. Tan, H. Xia, X. Wang, X. Qiao, P.K. Wong, Facile one-step synthesis of 3D hierarchical flower-like magnesium peroxide for efficient and fast removal of tetracycline from aqueous solution, *J. Hazard Mater.* 397 (2020), 122877.
- [44] C. Zhang, D. Qin, Y. Zhou, F. Qin, H. Wang, W. Wang, Y. Yang, G. Zeng, Dual optimization approach to Mo single atom dispersed g-C₃N₄ photocatalyst: Morphology and defect evolution, *Appl. Catal. B Environ.* 303 (2022).
- [45] Y. Wang, C. Zhu, G. Zuo, Y. Guo, W. Xiao, Y. Dai, J. Kong, X. Xu, Y. Zhou, A. Xie, C. Sun, Q. Xian, 0D/2D Co₃O₄/TiO₂ Z-Scheme heterojunction for boosted photocatalytic degradation and mechanism investigation, *Appl. Catal. B Environ.* 278 (2020).
- [46] Y. Bai, D. Wu, W. Wang, P. Chen, F. Tan, X. Wang, X. Qiao, P. Wong, Dramatically enhanced degradation of recalcitrant organic contaminants in MgO₂/Fe(III) Fenton-like system by organic chelating agents, *Environ. Res.* 192 (2020), 110242.
- [47] Z. Bao, L. Ye, B. Fang, L. Zhao, Synthesis of Fe_{0.32}Co_{0.68}/γ-Al₂O₃@C nanocomposite for depth treatment of dye sewage based on adsorption and advanced catalytic oxidation, *J. Mater. Chem. A* 5 (2017) 6664–6676.
- [48] P. Chen, L. Blaney, G. Cagnetta, J. Huang, B. Wang, Y. Wang, S. Deng, G. Yu, Degradation of ofloxacin by perylene diimide supramolecular nanofiber sunlight-driven photocatalysis, *Environ. Sci. Technol.* 53 (2019) 1564–1575.
- [49] Q. Ji, X. Cheng, Y. Wu, W. Xiang, H. He, Z. Xu, C. Xu, C. Qi, S. Li, L. Zhang, S. Yang, Visible light absorption by perylene diimide for synergistic persulfate activation towards efficient photodegradation of bisphenol A, *Appl. Catal. B Environ.* 282 (2021).
- [50] T. Wu, Q. He, Z. Liu, B. Shao, Q. Liang, Y. Pan, J. Huang, Z. Peng, Y. Liu, C. Zhao, X. Yuan, L. Tang, S. Gong, Tube wall delamination engineering induces photogenerated carrier separation to achieve photocatalytic performance improvement of tubular g-C₃N₄, *J. Hazard Mater.* 424 (2022), 127177.
- [51] F. Wang, Y. Feng, P. Chen, Y. Wang, Y. Su, Q. Zhang, Y. Zeng, Z. Xie, H. Liu, Y. Liu, W. Lv, G. Liu, Photocatalytic degradation of fluoroquinolone antibiotics using ordered mesoporous g-C₃N₄ under simulated sunlight irradiation: Kinetics, mechanism, and antibacterial activity elimination, *Appl. Catal. B Environ.* 227 (2018) 114–122.
- [52] Y. Li, Y. Fu, M. Zhu, Green synthesis of 3D tripyramid TiO₂ architectures with assistance of aloe extracts for highly efficient photocatalytic degradation of antibiotic ciprofloxacin, *Appl. Catal. B Environ.* 260 (2020).